UNIVERSITY *of York*

This is a repository copy of *Enhancement of collisionless shock ion acceleration by electrostatic ion two-stream instability in the upstream plasma*.

White Rose Research Online URL for this paper:
https://eprints.whiterose.ac.uk/id/eprint/145255/

Version: Published Version

Article:

White Rose
university consortium
Universities of Leeds, Sheffield & York

eprints@whiterose.ac.uk
https://eprints.whiterose.ac.uk/

Enhancement of collisionless shock ion acceleration by electrostatic ion two-stream instability in the upstream plasma

Rajesh Kumar,[1,*] Youichi Sakawa,[2] Leonard N. K. Döhl,[3] Nigel Woolsey,[3] and Alessio Morace[2]

[1]*Graduate School of Science, Osaka University, Toyonaka, Osaka 560-0043, Japan*
[2]*Institute of Laser Engineering, Osaka University, Suita, Osaka 565-0871, Japan*
[3]*Department of Physics, University of York, Heslington, York YO10-5DD, United Kingdom*

Ion acceleration in electrostatic collisionless shocks is driven by the interaction of the high-power laser with specially tailored near-relativistic critical density plasma. 2D EPOCH particle-in-cell simulations show that the ion acceleration is dependent on the target material used. In materials with low charge-to-mass ratio $\langle Z/A \rangle$, proton beams with high flux and low energy spread are generated. In multi-ion plasmas the ions with different $\langle Z/A \rangle$ acquire different velocities under a non-oscillating component of electrostatic field in the upstream region. This relative drift between the protons ($\langle Z/A \rangle = 1$) and the lower $\langle Z/A \rangle$ ions leads to the excitation of electrostatic ion two-stream instability. This in turn generates a low-velocity component in the upstream expanding protons. The velocity distribution of the upstream expanding protons is further broadened toward the higher velocity by the electrostatic ion two-stream instability between reflected protons, which results in large number of protons being accelerated by the shock.

I. INTRODUCTION

The development of high-intensity laser systems has opened a new era for laser-driven ions acceleration and there are several promising mechanisms for laser-driven ion acceleration. The energetic ion beams driven by laser-plasma interaction have many potential applications such as accelerator physics, cancer therapy, proton radiography, and inertial confinement fusion [1–3]. However, producing a proton beam with high energy, high flux, and low energy-spread proved to be the major challenge for practical applications [4,5]. Several mechanisms have been studied for laser-driven acceleration. At present, the most widely understood mechanism is Target Normal Sheath Acceleration (TNSA). This mechanism [6] and a related radiation-pressure hybrid-scheme [7] can drive protons to energies approaching 100 MeV. Alternative acceleration schemes, such as radiation-pressure acceleration that can achieve monoenergetic and higher energy suitable for applications impose strict and challenging conditions in experiments, such as the target thickness and laser contrast [8–10]. We describe a method to circumvent such constraints whilst providing methods to achieve higher ion energies.

Collisionless shock acceleration (CSA) has been proposed separately by Denavit [11] and Silva [12], with a detailed theoretical investigation complemented by Fiuza [13]. These studies suggest that a special near-critical density profile, N_{cr}, is important in order to control the sheath electric field, E_{TNSA}, at the plasma-vacuum interface. This in turn affects the ion spectrum in CSA. The E_{TNSA} amplitude can be reduced by using an exponentially decreasing density profile on the rear-side of the target [14], finally resulting in a quasimonoenergetic distribution for the CSA ions. CSA experiments using a linearly polarized CO_2 laser with near-N_{cr} gas-jet targets produced 20 MeV proton beam [15]. A number of experiments have been carried out over the last few years to understand and characterize ion acceleration via CSA [16–21]. One aspect of CSA that is currently not well understood for accelerating mono-energetic ions to high energies is the effect of the target material used.

In this paper we used the EPOCH particle-in-cell (PIC) open source code [22] to study the generation of electrostatic (ES) collisionless shocks and proton acceleration from shocks formed in plasmas of different material composition. Our results show that a low average charge-to-mass ratio ($\langle Z/A \rangle$) plasma produces a higher proton beam flux with a higher laser-to-proton energy conversion efficiency, and these differences become smaller at higher laser intensities. In the plasma with multi-ion species the ions with lower $\langle Z/A \rangle$ compared to the protons (with $\langle Z/A \rangle = 1$) gain different velocities. This results in difference between relative drift velocities of the protons and lower $\langle Z/A \rangle$ ions in the upstream region of the shock. This leads to the

*rajesh-dhiman@ile.osaka-u.ac.jp

excitation of an electrostatic ion two-stream instability (EITI) [23], which in turn enhances the number of the shock-accelerated protons [24]. To our best knowledge, most of the previous work has focused on shock formation [25–27] and ion heating [28–30]. This paper is the first investigation on the material (or $\langle Z/A \rangle$) dependence of EITI on CSA.

II. SIMULATIONS

We used 2D EPOCH simulations to investigate proton acceleration via CSA mechanism by modeling plasmas with different multi-ion compositions used commonly in experiments as target materials. The simulation box is 300×6 μm in size and composed of 9000×180 cells along the x- and y-axis respectively. Each cell contains 24–30 particles depending upon the material being studied. Open and periodic boundary conditions are used along the x- and y-axis respectively for both fields and particles.

The laser pulse and target in the PIC simulations use the parameters achievable at the Institute of Laser Engineering, Osaka University. An experiment would use the high intensity LFEX for the main interaction and the Gekko XII laser to preionize the target rear surface and create the necessary density profiles for CSA mechanism. The high intensity beam irradiated on the target front surface is linearly p-polarized with a temporal Gaussian profile of 1.5 ps full-width at half-maximum and peak intensity of 1.4×10^{19} W/cm^2 ($a_0 = 3.35$). The target consists of a tailored density profile increasing exponentially for 30 μm with 5 μm density scale length at N_{cr} on laser side, a 5 μm region of constant density at the relativistic critical density $a_0 N_{cr}$, and an exponentially decreasing density with 30 μm scale-length on the rear extending for 125 μm. The initial density profile is shown in Fig. 1(a), $t = 0$. The corresponding ion densities are configured to ensure quasineutrality. The density profile and laser parameters are the same for all materials. The different material compositions and associated $\langle Z/A \rangle$ used in this study are summarized in Table I. The simulations are timed to reach peak irradiance at 1.5 ps and have an initial electron and ion temperature of $T_e = T_i = 500$ eV.

A. Collisionless shock formation

Figure 1(a) shows the temporal evolution of N_H/N_{cr} in C$_2$H$_3$Cl for a number of times after the peak of the laser pulse, which enter the particle grid at 1.5 ps. During the time from $t = 0$ to $t = 1.75$ ps the laser interaction with plasma results in uniform electron heating via $J \times B$ [31]. This compresses the plasma in front of the exponentially decreasing density on the rear target side, as shown by the peak in the density profile in Fig. 1(a). As time evolves, the density on the target rear side is expanding, resulting in the formation of the ES collisionless shock. The shock propagates at velocity V_{sh} in the forward direction. The exponentially decreasing density profile in the upstream
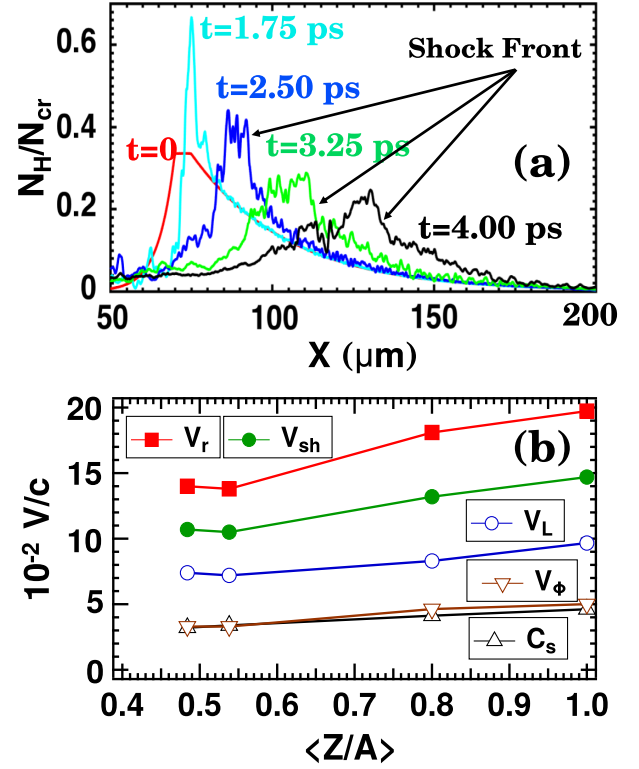

FIG. 1. (a) The temporal evolution of N_H/N_{cr} in C$_2$H$_3$Cl at $t = 0$, 1.75, 2.50, 3.25, and 4.00 ps. (b) $\langle Z/A \rangle$ dependence of the ion acoustic speed C_s, the lower threshold V_L, the shock speed V_{sh}, $V_\phi = \sqrt{2e\phi/m_p}$, and the velocity of the shock reflected protons V_r at $t = 4.0$ ps.

plasma, the region ahead of the shock results in a uniform ES sheath field ahead of the shock, $E_{TNSA} = T_e/eL_g$, where T_e is the upstream electron temperature, e is the electric charge, and L_g is the exponentially decreasing rear-side scale-length [14]. This E_{TNSA} field gives a uniform velocity V_0 to the upstream expanding protons.

For an ES collisionless shock to accelerate protons by ion reflection the ES potential ϕ at the shock must satisfy the relation $Ze\phi \geq \frac{1}{2}Am_p(V_{sh} - V_0)^2$, where $Z = A = 1$ for protons, and m_p is the proton mass [32]. Shock reflected protons have a velocity $V_r = 2V_{sh} - V_0$. ϕ can be estimated by subtracting the non-oscillating component of E_{TNSA} from the overall ES field (E_x) and integrating along the x-axis, $\phi = \int_\infty^x (E_x - E_{TNSA})dx$. At $t = 2.5$ ps, ϕ is large, as a result, acceleration of upstream protons via

TABLE I. The charge-to-mass ratio for different targets. Note, all ions are fully ionized except chlorine which has $Z_{Cl} = 15$.

Material	C$_2$H$_3$Cl	CH	He^{3}H	Hydrogen
$\langle Z/A \rangle$	0.4839	0.5385	0.8	1
$\langle Z \rangle$	30	7	4	1
$\langle A \rangle$	62	13	5	1

shock reflection occurs. By $t = 4.0$ ps, ϕ is gradually dissipating and reflection of protons becomes negligible.

Figure 1(b) compares the $\langle Z/A \rangle$ dependence of a number of velocities relative to the speed of light, c. Here $V_\phi = \sqrt{2e\phi/m_p}$ and $V_L = V_{sh} - V_\phi$ is the lower threshold for the proton reflection. The velocities V_r, V_{sh}, V_L, V_ϕ and the ion acoustic speed C_S show a general increase with $\langle Z/A \rangle$. The increasing velocities result from a $\sqrt{Z/A}$ dependence in the hole-boring velocity $V_{HB} = c\sqrt{\frac{Z}{2A}\frac{m_e}{m_p}\frac{N_{cr}}{N_e}a_0^2}$ with the nonrelativistic limit [33]. This is a good approximation for the low a_0 used. Here m_e is the electron mass, a_0 and N_e are the same for all the materials. The shock front moves forward at velocity V_{sh}, which is powered by the laser-driven hole boring process at the target front. As there is a rear surface density drop, V_{sh} increases in time. Protons with velocities V_0 that lie between V_L and V_{sh} are accelerated via shock reflection.

A 2D-relativistic Maxwellian $f(E) \propto E\exp(-E/T_e)$ is used for the electron energy spectrum in the upstream region. For all materials, $T_e \sim 2.0$ MeV. This implies that the ion acoustic speed is given by $C_s = \sqrt{ZT_e/Am_p}$ is only a function of $\langle Z/A \rangle$ as shown in Fig. 1(b).

Figures 2(a)–2(d) show the proton phase-space at 4.0 ps for each of the materials shown in Table I. The red solid line overlaid on each of the plots corresponds to the proton velocity distribution in the upstream region ahead of the shock front. This is integrated from the velocities within the vertical box in the phase-space plots, which spans across a range of $\Delta x = 3$ μm. The horizontal lines are the material dependent velocities V_r, V_{sh}, and V_L. Protons that satisfy the inequality $V_L \leq V_0 \leq V_{sh}$ are shock reflected. For target materials with lower $\langle Z/A \rangle$, such as C_2H_3Cl and CH, a significantly larger number of protons satisfy this inequality when compared to He^3H and H. As a result, a larger number of protons are shock accelerated. This is deduced by comparing Figs. 2(a) and 2(b) with Figs. 2(c) and 2(d). The proton velocity distribution is broader at lower $\langle Z/A \rangle$ due to the presence of the lower $\langle Z/A \rangle$ ions.

A broad velocity distribution results in a variation of the Mach number (M). To account for this we define $M = (V_{sh} - V_{mean})/C_s$, where V_{mean} is a mean value of V_0 in the distribution. In our calculations, we obtain $M = 1.6$–1.7 for all materials. This is in agreement with the critical Mach number ($M_{cr} = 1.6$), which has been previously validated in PIC simulations for linearly polarized laser pulse [11,13]. Therefore, the particle acceleration, and thus shock dissipation, is expected when the ions are being reflected. The maximum velocity of the reflected protons from the shock front is expected to reach $2V_{sh} - V_L$. Simulations show that the velocity distribution just ahead of the shock peaks around this maximum velocity. In the upstream plasma, protons with higher $\langle Z/A \rangle$ are preferentially accelerated in the x-direction by the ES field E_{TNSA}, which in turn drives the EITI.
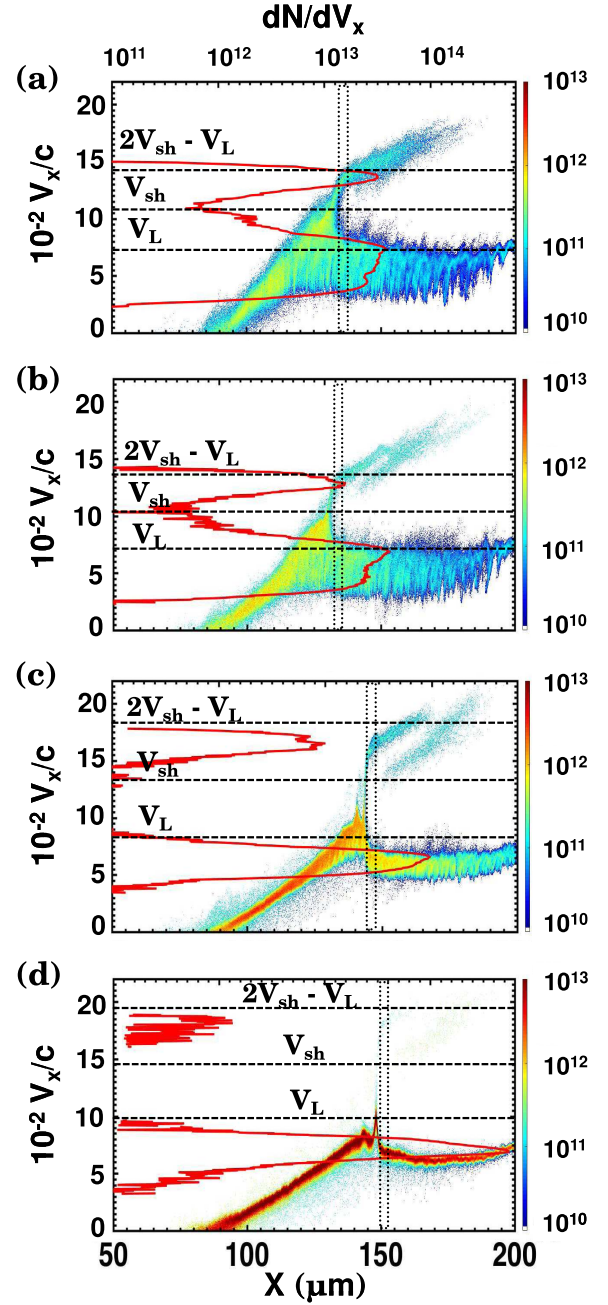

FIG. 2. A phase-space and velocity spectrum of the protons taken at $\Delta x = 3$ μm in the upstream of the shock front at $t = 4.0$ ps are shown for (a) C_2H_3Cl, (b) CH, (c) He^3H, and (d) Hydrogen.

Figure 3(a) shows the energy distribution of accelerated protons in the whole upstream region. We find that the energy spread increases with increasing $\langle Z/A \rangle$. Simulations show that this occurs at early times when ϕ is relatively weak. This is due to hole-boring on the front side of the target. These protons have a different velocity distribution and lower energies compared to the shock reflected protons, which results in the larger energy spread. The differences are apparent in Figs. 2(c) and 2(d).
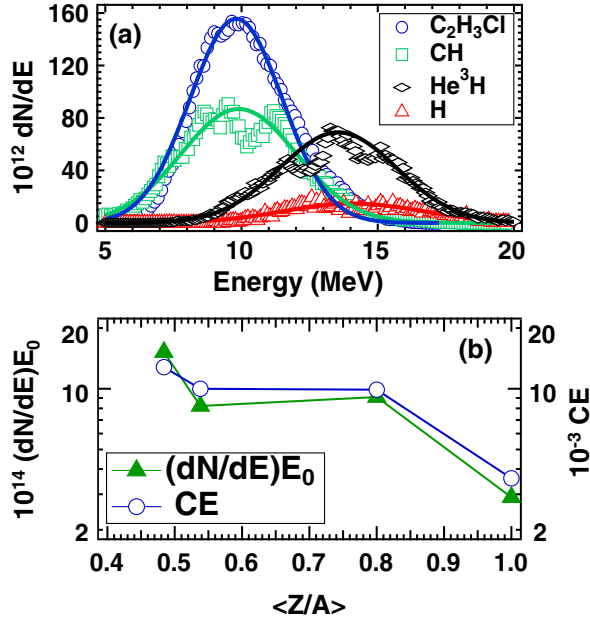
FIG. 3. (a) The energy spectra of the reflected protons in C_2H_3Cl (circles), CH (rectangles), He^3H (diamonds) and, H (triangles). (b) $\langle Z/A \rangle$ dependencies of the $(dN/dE)E_0$ and laser to the reflected protons conversion efficiency (CE) taken in the whole upstream region at $t = 4.0$ ps.

The energy distribution of the shock reflected protons multiplied by the peak energy in the distribution, E_0, is shown as a function of $\langle Z/A \rangle$ in Fig. 3(b). The laser-to-proton energy conversion efficiency (CE) is compared to the distribution in the same figure. Material with the lowest $\langle Z/A \rangle$ (C_2H_3Cl) show a CE almost an order of magnitude higher than a pure proton target with the highest $\langle Z/A \rangle$. In comparison, the peak energy of the distributions is increasing by a comparatively small factor of ~1.4 from C_2H_3Cl to H as shown in Fig. 3(a).

Figures 4(a) and 4(b) show the x-y spatial profile of the ES field, E_x, for the C_2H_3Cl upstream plasma. The simulation box size is $y = 6$ and $20~\mu m$, respectively. Both cases show a wavelike structure propagating in the x-direction, with increasing wavelength for larger x. The E_x profile along the x-axis is averaged along the y-axis and overlaid on the phase-space of the corresponding proton velocity distribution in the upstream shown in Fig 4(c). The modulation in E_x shows comparative correlation with the proton phase-space distributions. These modulations are caused by the EITI in the upstream plasma. This is excited by the relative drift velocity (v_d) between the two ion populations in plasmas with multi-ion species [23]. Our simulations show that this relative drift is driven by the E_{TNSA} in the upstream plasma which results in slower moving heavier ions with low $\langle Z/A \rangle$ and faster moving protons with high $\langle Z/A \rangle$. Simulations done by Zhang [26] have shown that in the transverse size-reduced simulation EITI propagates in the x-direction, whereas in the large transverse size simulation it propagates obliquely. In our
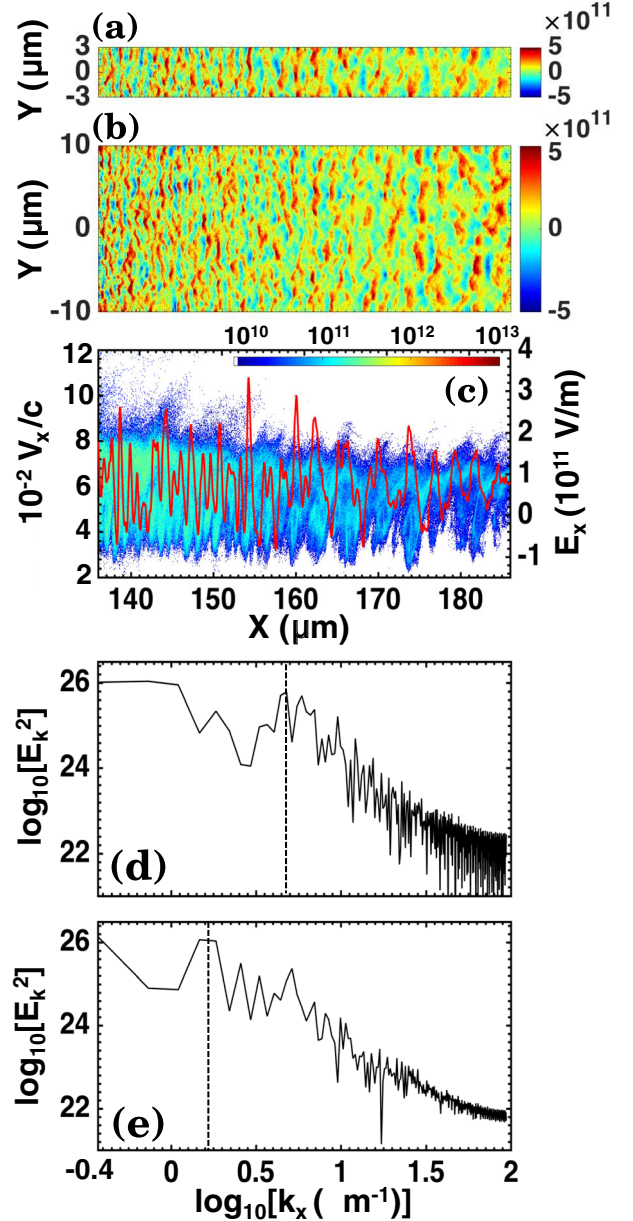

FIG. 4. 2D ES field (E_x) distribution averaged over two laser-cycles in the upstream region at $t = 4.0$ ps in C_2H_3Cl for the simulations box size of (a) $y = 6~\mu m$ and (b) $y = 20~\mu m$. (c) Phase-space of the upstream expanding protons and 1D profile of E_x. Derived power spectrum of E_x at $t = 4.0$ ps taken in the region of (d) $x = 135$–$145~\mu m$ and (e) $x = 165$–$175~\mu m$.

case, since the propagation directions of EITI are in the x-direction both for the small and the large transverse-size simulations [Figs. 4(a) and 4(b)], the instability is not oblique but longitudinal.

Temporal evolution of the upstream ion velocity distribution dN/dV_x in the C_2H_3Cl plasma is compared in Figs. 5(a) and 5(b). These plots were captured just ahead of the shock at $t = 2.0$ ps and 4.0 ps respectively. Initially, v_d is small and the instability has not established. As time
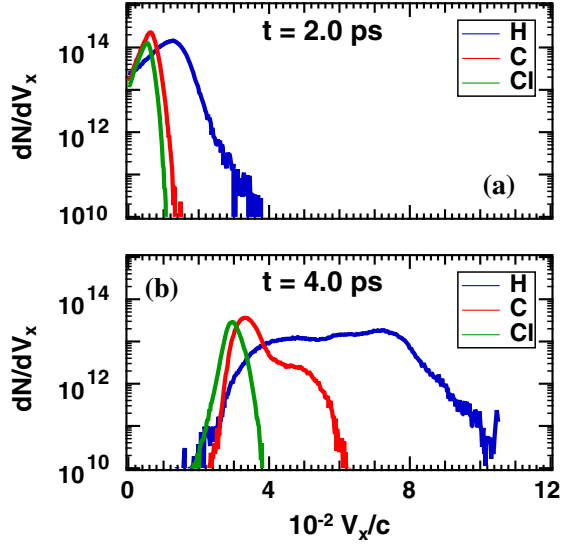
FIG. 5. Velocity spectrum of the expanding ions taken at $\Delta x = 3 \ \mu m$ in the upstream region at (a) $t = 2.0$ ps and (b) $t = 4.0$ ps in C_2H_3Cl.

FIG. 6. Time evolution of the expanding ion speed in C_2H_3Cl. The velocity of Cl-ions V_{Cl} (open circles) is derived from the peak of the velocity spectrum (dN/dV_{Cl}) taken at $\Delta x = 3 \ \mu m$ in the upstream region and fitted to logarithmic curve V_{Cl} (solid line). E_{TNSA} (dotted line) is derived from V_{Cl} and follows a $1/t$ dependence. Temporal variation of V_C (filled triangles) agrees well with the calculated V_C (V_{C-TNSA}, dashed line) from V_{Cl}. V_C^H (open triangles) shows the high-velocity tail of C-ions, which appears at $t = 2.5$ ps, and overlaps with the lower-velocity (V_H^L) (open rectangles) component of H-ions. V_H^H (filled rectangles) represents the higher-velocity component of H-ions, which is larger than the velocity calculated from E_{TNSA} [V_{H-TNSA}, (dot-dashed line)].

evolves, v_d increases, which leads to a growth in the instability. This results as shown in Fig. 5(b), in a high-velocity tail in the C-ion and a low-velocity component to the proton distributions. We note that the chlorine distribution does not broaden in time. This observation suggests that the broadening of proton distributions discussed in relation to Fig. 2 results from the EITI.

Temporal evolution of the velocity at the peak of the dN/dV_x distribution for Cl-ions, V_{Cl} (from the C_2H_3Cl target) is plotted in Fig. 6. V_{Cl} shows a logarithmic dependence with time indicating that V_{Cl} is determined by the upstream E_{TNSA}. By taking a derivative of a fit to the V_{Cl} distribution with $\langle Z/A \rangle = 0.429$, we infer that the time dependent E_{TNSA} evolves with a $1/t$ dependence as shown in Fig. 6. The temporal variations for V_{Cl} and E_{TNSA} relationship described by Mora [34]. The time dependence of the C-ion velocity (V_C) at the peak of dN/dV_x agrees well with calculations of V_C based on the inferred E_{TNSA} and $\langle Z/A \rangle = 0.5$ (V_{C-TNSA}). At $t = 2.5$ ps, a high-velocity tail (V_C^H) appears in V_C. This results from acceleration by an electric field associated with the EITI. The calculated velocity for H-ions from E_{TNSA} (V_{H-TNSA}) with $\langle Z/A \rangle = 1$, which gives the maximum possible velocity for H-ions caused by E_{TNSA}, is included for the comparison in Fig. 6. We approximate the simulated velocity distributions for protons as a sum of the three 1D-shifted Maxwellian's. These velocities, the lower (V_H^L), mean (V_H^M), and higher (V_H^H) velocity Maxwellian distributions are shown in Fig. 6. We note that V_C^H and V_H^L represent the EITI accelerated and decelerated C-ion and proton populations, respectively, and these populations have similar velocities. This occurs as an additional EITI develops due to the relative drift between the shock reflected proton population moving at approximately $2V_{sh} - V_0$, through the upstream expanding proton
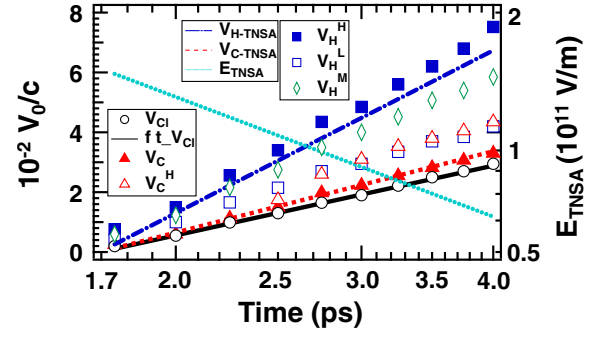
population moving at V_0. This further increases the number of protons satisfying the condition for CSA.

B. Electrostatic ion two-stream instability

In the cold plasma approximation, the dispersion relation for EITI is given by [30]

$$1 + \frac{1}{k_x^2 \lambda_{De}^2} = \frac{\omega_{p1}^2}{\omega^2} + \frac{\omega_{p2}^2}{(\omega - k_x v_d)^2}. \tag{1}$$

where k_x is the wave number in the x-direction, λ_{De} is the Debye length, ω_{p1} and ω_{p2} are the proton and heavy ion plasma frequencies, and v_d is the relative drift between the two ion populations. In multi-ion plasmas, ω_{p1} is the proton plasma frequency ω_{pp}, and ω_{p2} is the heavy-ion plasma frequency, as in, ω_{p2} is the carbon plasma frequency ω_{pc} for C_2H_3Cl and CH.

For C_2H_3Cl at $t = 4.0$ ps, the maximum amplitude of the modulation in E_x in the region of $x = 135-145 \ \mu m$ occurs at $k_x = 4.7 \times 10^6 \ m^{-1}$ [dashed line in Fig. 4(d)], and $\lambda_{De} = 0.4 \ \mu m$ (for $N_e = 6.5 \times 10^{20} \ cm^{-3}$ and $T_e = 2$ MeV) at $x = 140 \ \mu m$ in the upstream region. This results in $k_x \lambda_{De} > 1$, enabling us to neglect the second term on the left-hand side of Eq. (1). At $x = 140 \ \mu m$, the carbon ion and proton number densities are $N_C = 4 \times 10^{19} \ cm^{-3}$ and $N_p = 1.3 \times 10^{20} \ cm^{-3}$ giving $\omega_{pc} = \omega_{pp} = 1.5 \times 10^{13} \ sec^{-1}$. Equation (1) has an unstable solution with the maximum growth rate of $\sim \omega_{pc}/2$ at $k_x \sim \sqrt{3} \omega_{pc}/v_d$. We take $v_d = V_H^H - V_C = 0.042c$ at $t = 4.0$ ps. This gives, $k_x \sim 2.1 \times 10^6 \ m^{-1}$,

which agrees relatively well with the value of $k_x = 4.7 \times 10^6$ m^{-1} extracted from simulation. We refer to this as heavy-ion EITI.

At $x = 160$ μm, $N_C = 1 \times 10^{19}$ cm^{-3}, which gives $\omega_{pc} = 7.2 \times 10^{12}$ sec^{-1}, and $v_d = 0.040c$ at $t = 4.0$ ps. Thus, $k_x \sim 1.0 \times 10^6$ m^{-1}, which is comparable to $k_x \sim 1.6 \times 10^6$ m^{-1} as shown in simulation in Fig. 4(e). Hence, it is clear from Figs. 4(d) and 4(e), k_x decreases as x increases because the plasma density decreases as shown in Fig. 1(a) ($t = 4.0$ ps).

At $t > 2.5$ ps, the number of protons reflected by the shock front increases, which contributes to the excitation of the EITI between the expanding and the reflected protons. This is referred to as reflected-proton EITI. This leads to the generation of a high-velocity tail in V_H^H in the upstream plasma. In the case of reflected-proton EITI, $\omega_{p1} = \omega_{pp}$ and ω_{p2} is the reflected proton plasma frequency ω_{pref}. As shown in Fig. 2(a), the number of reflected protons is smaller than that of the expanding protons even at $t = 4.0$ ps. Hence, $\omega_{pref} < \omega_{pp}$. The maximum growth rate of reflected-proton EITI [30] is $\sim (3\sqrt{3}(N_{ref}/N_{exp})/16)^{1/3}\omega_{pp}$ at $k_x \sim \omega_{pp}/v_d^r$. The relative drift between the reflected and expanding protons is $v_d^r = 0.064c$ at $x = 140$ μm and $t = 4.0$ ps. Therefore, $k_x \sim 6.8 \times 10^5$ m^{-1}, which is comparable to the k_x value for the maximum growth rate of heavy-ion EITI at $x = 140$ μm by a factor of 0.31. As a result, this suggests both that heavy-ion and reflected-proton EITIs occur with similar growth rates and wave numbers.

V_{H-TNSA} or the maximum possible velocity of H-ions accelerated by E_{TNSA} in C$_2$H$_3$Cl is shown in Fig. 6. We infer that a large number of protons is accelerated by the wave electric field of reflected-proton EITI and obtain the expansion velocity V_0 larger than V_{H-TNSA}. This acceleration generates a significant number of expanding protons with the velocities larger than V_L, and results in the enhancement of the shock accelerated protons. Simulation studies done by Grassi et al. [35], have shown that the development of ion turbulence in H plasma leads to the heating of upstream ions, which allows a fraction of ions to exceed the threshold for ion reflection from the shock front.

To confirm the effect of $\langle Z/A \rangle$ on EITI, PIC-simulations with the same laser and density properties used throughout are compared to fully ionized carbon deuterium (CD) plasma. As shown in Fig. 7(a), since both C and D-ions have the same $\langle Z/A \rangle = 0.5$, both ions are accelerated by E_{TNSA} in the upstream plasma, and there is no relative drift between them, as in, $v_d = 0$. Therefore, no instability is excited, and no broadening of the upstream ions occurs. In multi-ion plasmas, a high-velocity tail and a low-velocity component appear in the smaller and larger $\langle Z/A \rangle$ ions, respectively. Figure 7(b) represents upstream ion velocity distribution for CCl$_2$ plasma with fully ionized C and
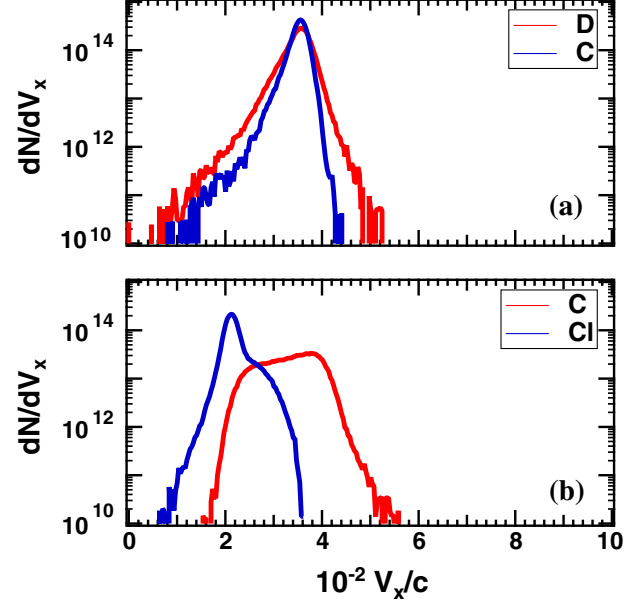

FIG. 7. Velocity spectrum of the expanding ions in (a) CD and (b) CCl$_2$ targets taken at $\Delta x = 3$ μm in the upstream region at $t = 4.0$ ps.

$Z_{Cl} = 10$. A high-velocity tail in Cl-ions and a low-velocity component of C-ions appear because of heavy-ion EITI.

III. DISCUSSION AND SUMMARY

We further generalize our results by finding the dependence of the peak energy of the reflected protons and proton flux on the laser intensity corresponding to the $a_0 = 3.35$, 10, and 33. In order to compensate for relativistically induced transparency, the initial electron density is varied
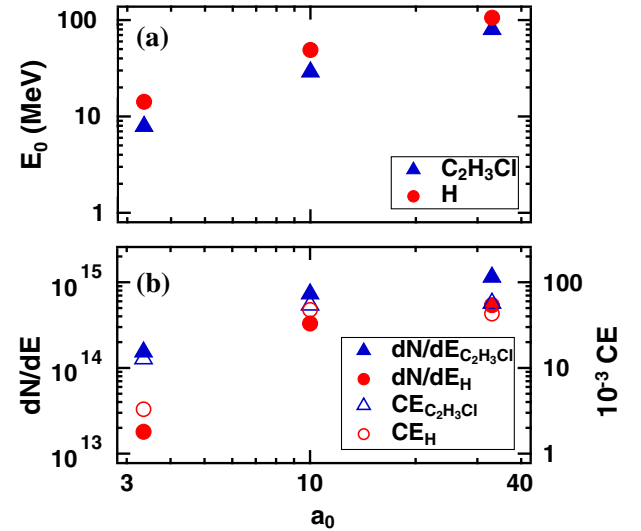

FIG. 8. (a) The peak energy E_0 of the shock reflected protons (b) the laser to proton conversion efficiency (CE) and the number of the shock accelerated protons dN/dE at E_0 in C$_2$H$_3$Cl and H plasmas.

for different laser intensities by $a_0 N_{cr}$ for all plasmas. Figure 8 represents the peak energy (E_0), conversion efficiency (CE), and number (dN/dE at E_0) of the shock accelerated protons for different laser intensities corresponding to $a_0 = 3.35$, 10, and 33 in C_2H_3Cl and H plasmas. For C_2H_3Cl plasma, E_0, dN/dE, and CE increase with increasing laser intensity. However for H plasma, E_0 and dN/dE increase but CE first increases and then decreases with increasing laser intensity. The E_0, dN/dE, and CE are always larger for C_2H_3Cl plasma compared to H plasma. As shown in Fig. 8(b), the increment in the dN/dE and CE for the higher laser intensity is different from the lower laser intensity, whereas dN/dE and CE of the shock accelerated protons are always higher in lower $\langle Z/A \rangle$ (C_2H_3Cl) plasma than pure H plasma. At lower laser intensity ($a_0 = 3.35$), these increments are found to be ∼8.6 and ∼4, while at higher laser intensity ($a_0 = 33$), these increments are found to be ∼2 and ∼1.3.

We have performed the 2D PIC simulations in a plane wave approximation with an infinite spot-size. In the 3D scenario a smaller amplitude TNSA field will appear on the rear-side of the target according to Xiao *et al.* [36], which results in a quasimonoenergetic distribution for the CSA ions [14]. Even with this small amplitude TNSA field, the ions with different $\langle Z/A \rangle$ will be accelerated to the different velocities. This leads to the development of EITI in multi-ion species plasma.

In summary, we have presented a PIC simulation study of the ES collisionless shock proton acceleration in different target materials. Protons with high flux and narrower energy spread can be produced using the lower $\langle Z/A \rangle$ materials. The excitation of heavy-ion EITI leads to a large velocity spread in the upstream region of protons in multi-ion materials. The velocity distribution of the upstream expanding protons is further broadened toward the higher velocity by the EITI between reflected protons. As a result, a larger number of protons are driven by collisionless shock acceleration mechanism. This work supports future experimental work and investigations to a complete understanding of EITI and collisionless shocks using accessible experimental parameters.

[1] H. Daido, M. Nishiuchi, and A. S. Pirozhkov, Review of laser-driven ion sources and their applications, Rep. Prog. Phys. **75,** 056401 (2012).

[2] A. Macchi, M. Borghesi, and M. Passoni, Ion acceleration by superintense laser-plasma interaction, Rev. Mod. Phys. **85,** 751 (2013).

[3] M. Roth, T. E. Cowan, M. H. Key, S. P. Hatchett, C. Brown, W. Fountain, J. Johnson, D. M. Pennington, R. A. Snavely, S. C. Wilks, K. Yasuike, H. Ruhl, P. Pegoraro, S. V. Bulanov, E. M. Campbell, M. D. Perry, and H. Powell, Fast Ignition by Intense Laser-Accelerated Proton Beams, Phys. Rev. Lett. **86,** 436 (2001).

[4] S. V. Bulanov, T. Z. Esirkepov, V. S. Khororshkov, A. Z. Kuznetsov, and F. Pegoraro, Oncological hadron-therapy with laser ion accelerators, Phys. Lett. A **299,** 240 (2002).

[5] U. Linz and J. Alonso, What will it take for laser driven proton accelerators to be applied to tumor therapy?, Phys. Rev. ST Accel. Beams **10,** 094801 (2007).

[6] F. Wagner, O. Deppert, C. Brabetz, P. Fiala, A. Kleinschmidt, P. Poth, V. A. Schanz, A. Tebartz, B. Zielbauer, M. Roth, T. Stohlker, and V. Bagnoud, Maximum Proton Energy above 85 MeV from the Relativistic Interaction of Laser Pulses with Micrometer Thick CH_2 Targets, Phys. Rev. Lett. **116,** 205002 (2016).

[7] A. Higginson, R. J. Gray, M. King, R. J. Dance, S. D. R. Williamson, N. M. H. Butler, R. Wilson, R. Capdessus, C. Armstrong, J. S. Green, S. J. Hawkes, P. Martin, W. Q. Wei, S. R. Mirfayzi, X. H. Yuan, S. Kar, M. Borghesi, R. J. Clarke, D. Neely, and P. McKenna, Near-100 MeV protons via a laser-driven transparency-enhanced hybrid acceleration scheme, Nat. Commun. **9,** 724 (2018).

[8] I. J. Kim, K. H. Pae, W. Choi, C. L. Lee, H. T. Kim, H. Singhal, J. H. Sung, S. K. Lee, H. W. Lee, P. V. Nickles, T. M. Jeong, C. M. Kim, and C. H. Nam, Radiation pressure acceleration of protons to 93 MeV with circularly polarized petawatt laser pulses, Phys. Plasmas **23,** 070701 (2016).

[9] F. Dollar, C. Zulick, A. Raymond, V. Chvykov, L. Willingale, V. Yanovsky, A. Maksimchuk, A. G. R. Thomas, and K. Krushelnick, Enhanced laser absorption from radiation pressure in intense laser plasma interactions, New J. Phys. **19,** 063014 (2017).

[10] A. Henig, S. Steinke, M. Schnurer, T. Sokollik, R. Horlein, D. Kiefer, D. Jung, J. Schreiber, B. M. Hegelich, X. Q. Yan, J. Meyer-ter-Vehn, T. Tajima, P. V. Nickles, W. Sandner, and D. Habs, Radiation-Pressure Acceleration of Ion Beams Driven by Circularly Polarized Laser Pulses, Phys. Rev. Lett. **103,** 245003 (2009).

[11] J. Denavit, Absorption of High-Intensity Subpicosecond Lasers on Solid Density Targets, Phys. Rev. Lett. **69,** 3052 (1992).

[12] L. O. Silva, M. Marti, J. R. Davies, R. A. Fonseca, C. Ren, F. S. Tsung, and W. B. Mori, Proton Shock Acceleration in Laser-Plasma Interactions, Phys. Rev. Lett. **92,** 015002 (2004).

[13] F. Fiuza, A. Stockem, E. Boella, R. A. Fonseca, L. O. Silva, D. Haberberger, S. Tochitsky, C. Gong, W. B. Mori, and C. Joshi, Laser-Driven Shock Acceleration of Monoenergetic Ion Beams, Phys. Rev. Lett. **109,** 215001 (2012).

[14] T. Grismayer and P. Mora, Influence of a finite initial ion density gradient on plasma expansion into a vacuum, Phys. Plasmas **13,** 032103 (2006).

[15] D. Haberberger, S. Tochitsky, F. Fiuza, C. Gong, R. A. Fonseca, L. O. Silva, W. B. Mori, and C. Joshi, Collisionless shocks in laser-produced plasma generate monoenergetic high-energy proton beams, Nat. Phys. **8,** 95 (2012).

[16] P. Antici, E. Boella, S. N. Chen, D. S. Andrews, M. Barberio, J. Bker, F. Cardelli, J. L. Feugeas, M. Glesser, P. Nicola, L. Romagnani, M. Scisci, M. Starodubtsev, O. Willi, J. C. Kieffer, V. Tikhonchuk, H. Ppin, L. O. Silva, E. d Humires, and J. Fuchs, Acceleration of collimated 45 MeV protons by collisionless shocks driven in low-density, large-scale gradient plasmas by a 10^{20} W/cm^2, 1 μm laser, Sci. Rep. **7,** 16463 (2017).

[17] A. Pak, S. Kerr, N. Lemos, A. Link, P. Patel, F. Albert, L. Divol, B. B. Pollock, D. Haberberger, D. Froula, M. Gauthier, S. H. Glenzer, A. Longman, L. Manzoor, R. Fedosejevs, S. Tochitsky, C. Joshi, and F. Fiuza, Collisionless shock acceleration of narrow energy spread ion beams from mixed species plasmas using 1 μm lasers, Phys. Rev. Accel. Beams **21,** 103401 (2018).

[18] H. Zhang, B. F. Shen, W. P. Wang, S. H. Zhai, S. S. Li, X. M. Lu, J. F. Li, R. J. Xu, X. L. Wang, X. Y. Liang, Y. X. Leng, R. X. Li, and Z. Z. Xu, Collisionless Shock Acceleration of High-Flux Quasimonoenergetic Proton Beams Driven by Circularly Polarized Laser Pulses, Phys. Rev. Lett. **119,** 164801 (2017).

[19] O. Tresca, N. P. Dover, N. Cook, C. Maharjan, M. N. Polyanskiy, Z. Najmudin, P. Shkolnikov, and I. Pogorelsky, Spectral Modification of Shock Accelerated Ions Using a Hydrodynamically Shaped Gas Target, Phys. Rev. Lett. **115,** 094802 (2015).

[20] H. Zhang, B. F. Shen, W. P. Wang, Y. Xu, Y. Q. Liu, X. Y. Liang, Y. X. Leng, R. X. Li, X. Q. Yan, J. E. Chen, and Z. Z. Xu, Collisionless shocks driven by 800 nm laser pulses generate high-energy carbon ions, Phys. Plasmas **22,** 013113 (2015).

[21] M. Liu, S. M. Weng, Y. T. Li, D. W. Yuan, M. Chen, P. Mulser, Z. M. Sheng, M. Murakami, L. L. Yu, X. L. Zheng, and J. Zhang, Collisionless electrostatic shock formation and ion acceleration in intense laser interactions with near critical density plasmas, Phys. Plasmas **23,** 113103 (2016).

[22] T. D. Arber, K. Bennett, C. S. Brady, A. L. Douglas, M. G. Ramsay, N. J. Sircombe, P. Gillies, R. G. Evans, H. Schmitz, A. R. Bell, and C. P. Ridger, Contemporary particle-in-cell approach to laser-plasma modelling, Plasma Phys. Controlled Fusion **57,** 113001 (2015).

[23] H. Karimabadi, N. Omidi, and K. Quest, Two-dimensional simulations of the ion/ion acoustic instability and electrostatic shocks, Geophys. Res. Lett. **18,** 1813 (1991).

[24] G. Sarri, G. C. Murphy, M. E. Dieckmann, A. Bret, K. Quinn, I. Kourakis, M. Borghesi, L. Drury, and A. Ynnerman, Two-dimensional particle-in-cell simulation of the expansion of a plasma into a rarefied medium, New J. Phys. **13,** 073023 (2011).

[25] H. G. Rinderknecht, H. S. Park, J. S. Ross, P. A. Amendt, D. P. Higginson, S. C. Wilks, D. Haberberger, J. Katz, D. H. Froula, N. M. Hoffman, G. Kagan, B. D. Keenan, and E. L. Vold, Highly Resolved Measurements of a Developing Strong Collisional Plasma Shock, Phys. Rev. Lett. **120,** 095001 (2018).

[26] W. S. Zhang, H. B. Cai, and S. P. Zhu, The formation and dissipation of electrostatic shock waves: the role of ion–ion acoustic instabilities, Plasma Phys. Controlled Fusion **60,** 055001 (2018).

[27] M. King, R. J. Gray, H. W. Powell, R. Capdessus, and P. Mckenna, Energy exchange via multi-species streaming in laser-driven ion acceleration, Plasma Phys. Controlled Fusion **59,** 014003 (2017).

[28] J. S. Ross, H.-S. Park, R. Berger, L. Divol, N. L. Kugland, W. Rozmus, D. Ryutov, and S. H. Glenzer, Collisionless Coupling of Ion and Electron Temperatures in Counter-streaming Plasma Flows, Phys. Rev. Lett. **110,** 145005 (2013).

[29] T. N. Kato and H. Takabe, Electrostatic and electromagnetic instabilities associated with electrostatic shocks: Two-dimensional particle-in-cell simulation, Phys. Plasmas **17,** 032114 (2010).

[30] Y. Ohira and F. Takahara, Oblique ion two-stream instability in the foot region of a collisionless shock, Astrophys. J. **688,** 320 (2008).

[31] W. L. Kruer and K. G. Estabrook, J×B heating by very intense laser light, Phys. Fluids **28,** 430 (1985).

[32] D. A. Tidman and N. A. Krall, *Shock Waves in Collisionless Plasmas* (Wiley-Interscience, New York, 1971).

[33] A. P. L. Robinson, D. Neely, P. McKenna, and R. G. Evans, Spectral control in proton acceleration with multiple laser pulses, Plasma Phys. Controlled Fusion **49,** 373 (2007).

[34] P. Mora, Plasma Expansion into a Vacuum, Phys. Rev. Lett. **90,** 185002 (2003).

[35] A. Grassi, L. Fedeli, A. Sgattoni, and A. Macchi, Vlasov simulation of laser-driven shock acceleration and ion turbulence, Plasma Phys. Controlled Fusion **58,** 034021 (2016).

[36] K. D. Xiao, C. T. Zhou, K. Jiang, Y. C. Yang, R. Li, H. Zhang, B. Qiao, T. W. Huang, J. M. Cao, T. X. Cai, M. Y. Yu, S. C. Ruan, and X. T. He, High Z neoclassical transport: Application and limitation of analytical formulae for modelling JET experimental parameters, Phys. Plasmas **25,** 012303 (2018).